Supporting Information

Inorganic Frameworks of Low-Dimensional Perovskites Dictate the Performance and Stability of Mixed-Dimensional Perovskite Solar Cells

Benny Febriansyah,[a],[b] Yongxin Li,[c] David Giovanni,[d] Teddy Salim,[e] Thomas J. N. Hooper,[f] Ying Sim,[b],[g] Daphne Ma,[e] Shoba Laxmi,[c] Yulia Lekina,[d] Teck Ming Koh,[b] Ze Xiang Shen,[d] Sumod A. Pullarkat,[c] Tze Chien Sum,[d] Subodh G. Mhaisalkar,[b],[e] Joel W. Ager,[a],[h] and Nripan Mathews*[b],[e],[g]*

[a] Dr. B. Febriansyah, Prof. J. W. Ager
Berkeley Educational Alliance for Research in Singapore (BEARS), Ltd.
1 CREATE Way, Singapore 138602, Singapore
E-mail: jwager@berkeley.edu

[b] Dr. B. Febriansyah, Dr. Y. Sim, Dr. T. M. Koh, Prof. S. G. Mhaisalkar, Prof. N. Mathews
Energy Research Institute at Nanyang Technological University (ERI@N)
50 Nanyang Drive, Singapore 637553, Singapore
E-mail: nripan@ntu.edu.sg

[c] Dr Y. Li, S. Laxmi, Dr. S. A. Pullarkat
Chemistry and Biological Chemistry, School of Physical and Mathematical Sciences, Nanyang Technological University
21 Nanyang Link, Singapore 637371, Singapore

[d] Dr. D. Giovanni, Dr. Y. Lekina, Prof. T. C. Sum, Prof. Z. X. Shen
Division of Physics and Applied Physics, School of Physical and Mathematical Sciences, Nanyang Technological University
21 Nanyang Link, Singapore 637371, Singapore

[e] Dr. T. Salim, Dr. D. Ma, Prof. S. G. Mhaisalkar, Prof. N. Mathews
School of Materials Science and Engineering, Nanyang Technological University
50 Nanyang Avenue, Singapore 639798, Singapore

[f] Dr. T. J. N. Hooper
Centre of High Field Nuclear Magnetic Resonance (NMR) Spectroscopy and Imaging, Nanyang Technological University
21 Nanyang Link, Singapore 637371, Singapore

[g] Dr. Y. Sim, Prof. Nripan Mathews
Singapore-CEA Alliance for Research in Circular Economy (SCARCE), Nanyang Technological University
62 Nanyang Drive, Singapore 637459, Singapore

[h] Prof. J. W. Ager
Department of Materials Science and Engineering, University of California at Berkeley,
Berkeley, California 94720, USA

Keywords: mixed-dimensional perovskite, perovskite solar cells, intra-octahedral distortion, thermal stability, crystal engineering

Experimental methods

Materials synthesis

Chemicals. Aqueous hydroiodic acid (57 wt. %, distilled, 99.999%), 2-phenethylamine (≥99%), 4-fluorophenethylamine (99%), 4-(2-aminoethyl)pyridine (96%), 4-nitrophenethylamine hydrochloride (95%), pyridine (anhydrous, 99.8%), 2-(4-hydroxyphenyl)ethylamine (≥98.0%), 1-iodopropane (99%), 4-(2-aminoethyl)aniline (97%), cesium iodide (99.999% trace metals basis), tin(II) chloride dihydrate (≥99.995% trace metals basis), indium(III) chloride (anhydrous, powder, ≥99.999% trace metals basis), 4-*tert*-butylpyridine (98%), bis(trifluoromethane)sulfonimide lithium salt (Li-TFSI; 99.95 %), anhydrous chlorobenzene, acetonitrile, 2-propanol, dimethylformamide (DMF) and *N*-methyl-2-pyrrolidone (NMP) were obtained from Sigma-Aldrich. Pb(II) iodide (99.99%, trace metals basis) was bought from TCI chemicals, while formamidinium iodide and N^2,N^2,$N^{2'}$,$N^{2'}$,N^7,N^7,$N^{7'}$,$N^{7'}$-octakis(4-methoxyphenyl)-9,9'-spirobi[9*H*-fluorene]-2,2′,7, 7′-tetramine (Spiro-OMeTAD) were purchased from Greatcell Solar Materials and LumTec, respectively. Ethanol was obtained from Alfa Aesar and diethyl ether from Schedelco. All reagents were used without purification unless otherwise stated in associated procedure.

General procedure used to synthesize the ammonium iodide salts. To an ice cooled round-bottom flask containing ethanol (typically 20 mL) and the requisite amine (*i.e.,* 4-fluorophenethylamine (1.00 g; 7.19 mmole) for FPEAI; 4-(2-aminoethyl)pyridine (1.00 g; 8.18 mmole) for $PyrEAI_2$; 4-(2-aminoethyl)aniline (1.00 g; 7.34 mmole) for NH_3PEAI_2; 2-phenethylamine (1.00 g; 8.25 mmole) for PEAI; and 2-(4-hydroxyphenyl)ethylamine (1.00 g; 7.29 mmole) for OHPEAI) was added a stoichiometric amount concentrated hydroiodic acid (2 equivalent in the case of $PyrEAI_2$ and NH_3PEAI_2). After stirring the resulting mixture for 1 hour, all volatiles were removed using a rotary evaporator. The solids, thereby, obtained were washed with copious amounts of diethyl ether and dried under vacuum, overnight, at 50 °C. The resulting powders were subsequently transferred to argon-filled glovebox for storage. Nuclear magnetic resonance (NMR) spectroscopy was used to confirm the identity and purity of the compounds synthesized.

***N*-propyl pyridinium iodide ((PrPyr)I).** A flamed-dried two-neck round-bottom flask was charged with a stoichiometric amount of pyridine (1.0 g; 12.64 mmole) and 1-iodopropane

(2.15 g; 12.64 mmole). Subsequent to degassing *via* the freeze-pump-thaw method, anhydrous acetonitrile (25 mL, dried with CaH_2 before being distilled) added and the resulting mixture was stirred at reflux for *ca.* 48 hrs, until reaction was complete. This was assessed by 1H NMR spectroscopy. Upon cooling, the precipitate formed during reaction was isolated by filtration, thoroughly washed with diethyl ether, and dried under vacuum to give the target compounds.

Growth of single crystals of hybrid low-dimensional perovskites. In general, stoichiometric amounts of PbI_2 (0.12 g; 0.25 mmole) and organic halide salt (*i.e.,* FPEAI (0.13 g; 0.50 mmole), $PyrEAI_2$ (0.09 g; 0.25 mmole), NO_2PEACl (0.10 g; 0.50 mmole), NH_3PEAI_2 (0.20 g; 0.50 mmole), PEAI (0.12 g; 0.50 mmole), OHPEAI (0.13 g; 0.50 mmole), were added to sufficient concentrated aqueous HI (stabilized through addition of 5 % H_3PO_2, v/v relative to HI) to give 0.25 – 0.30 M concentrations of Pb^{2+}. The resulting mixtures were heated, with stirring, under an N_2 atmosphere, at 130 – 140 °C for approximately 30 mins until clear solutions were obtained. Subsequent *slow* cooling to room temperature afforded single crystals suitable for X-ray crystallography. The single crystals (*i.e.,* $(FPEA)_2PbI_4$, $(PyrEA)PbI_4$, $(NO_2PEA)_2PbI_4$, $(NH_3PEA)_2PbI_6$, $(PEA)_2PbI_4$, and $(OHPEA)_2PbI_4$) were then filtered, washed with degassed anhydrous diethyl ether, and transferred to an inert atmosphere glovebox for storage and handling. As for $(PrPyr)PbI_3$, the single crystal was grown from a concentrated DMSO solution containing stoichiometric amounts of PbI_2 (0.12 g; 0.25 mmole) and PrPyrI (0.06 g; 0.25 mmole) *via* the vapour diffusion method. Antisolvent used was acetone and the crystals obtained in this manner were then removed by filtration and dried. Single crystals suitable for X-ray crystallography were, typically, obtained within 1 – 2 weeks.

Thin films fabrication of three-dimensional (3D) and mixed-dimensional perovskites. Thin films used in characterization of the structural, morphological, compositional and optical properties were prepared *via* the following procedure. Prior use, the substrates (glass or patterned FTO) were pre-cleaned by sequential sonication for 15 min periods each in soap solution (Decon), deionized water, acetone, ethanol, and isopropanol, followed by ozone plasma treatment for 15 mins. Separately, 0.25 M solutions containing PbI_2, FAI, and CsI (in a 1.05 : 0.85 : 0.15 ratio), with or without the addition of 2.5 mole% (relative to 3D perovskite) of hybrid low-dimensional perovskites (synthesized previously), were prepared by dissolving the precursors in a 4:1 mixture of DMF and NMP. 2.5 mole% was chosen because it was found that with such amount, the most optimized device performance could be achieved, especially

with FPEA (**Figure S12**). Accordingly, the same stoichiometry was applied to low-dimensional materials templated by other bulky cations (PyrEA, NO_2PEA, PrPyr, NH_3PEA, PEA, and OHPEA) as well in order to provide a fair comparison across the series of the organics and to minimize other possible side effects (e.g., crystallization seeding effect or compositional distribution variation) that could have arisen due to the different amounts used. The solutions were then filtered and spincoated in a two-steps program (10 s at 1000 rpm, acceleration 200 rpm s^{-1} followed by 10 s at 6000 rpm, acceleration: 6000 rpm s^{-1}) onto pre-cleaned substrates. During the second step, 100 μL of chlorobenzene was introduced on the spinning substrate 5 s prior to the end of the program. In order to remove residual solvents and promote crystal growth, the resulting films were then heated at 105 °C for 30 mins. As for surface-treated samples (for depth-profiling X-ray photoelectron spectroscopy study), dilute solutions of iodide salts of cations 4-fluorophenethylammonium (FPEA), 4-(2-ammoniumethyl)pyridinium (PyrEA), 4-nitrophenethylammonium (NO_2PEA), *N*-propyl pyridinium (PrPyr), or 4-(2-ammoniumethyl)anilinium (NH_3PEA) (2.5 mM in isopropanol) are deposited onto perovskite films at 4000 rpm for 30 s, followed by annealing at 100 °C for 15 min.

Solar cell device fabrication. The planar solar cells in this study are based on compact SnO_2 as the electron transporting layer. The SnO_2 film was deposited *via* spincoating of indium-doped ethanolic $SnCl_2$ solution. Briefly, $SnCl_2{\cdot}2H_2O$ was dissolved in ethanol at 0.05 M concentration, followed by stirring for 5 mins. Ethanolic $InCl_3$ solution (20 uL, 0.4 mmole %) was then added before the resulting mixture was further sonicated for at least 5 mins and spin coated on top of UV-treated pre-cleaned substrates in a two-steps program (10 s at 1000 rpm, acceleration 200 rpm s^{-1} followed by 10 s at 6000 rpm, acceleration: 6000 rpm s^{-1}). After that, the resulting films were pre-dried at 80 °C for 10 min and annealed at 180 °C for 1 hour. UV-ozone treatment was done for 15 min for SnO_2 layers before deposition of perovskite films. The perovskite layer was prepared by spin coating 1.35 M solutions of $FA_{0.85}Cs_{0.15}PbI_3$ (with or without low-dimensional perovskite additives) in DMF-NMP, based on Pb^{2+}, with similar spin-coating parameters to the thin-film fabrication step. Subsequently, the substrate was placed on a hot plate to anneal at 105 °C for 30 mins. After cooling to room temperature, solution of hole-transporting material Spiro-OMeTAD was sequentially deposited onto the perovskite films by dynamic spin-coating at 4000 rpm for 30 s. The Spiro-OMeTAD solutions were prepared by dissolving Spiro-OMeTAD in chlorobenzene (70 mg ml^{-1}) and adding tert-

butylpyridine (28 μL) and lithium bis(trifluoromethylsulfonyl)imide (520 mg ml^{-1} in acetonitrile, 17 μL) to it. Finally, gold electrode with approximately 100 nm of thickness was deposited with a mask with device area of 0.09 cm^2 using a thermal evaporator.

Instrumentations and methods

Structural characterization

Glancing angle X-ray diffraction (GAXRD). GAXRD measurements were conducted using a Bruker AXS D8 ADVANCE system with CuKα radiation (λ = 1.5418 Å). The XRD spectra were recorded with an incident angle of 4°, a step size of 0.05° and a delay time of 1 s for each step.

X-ray Crystallography. Crystals were mounted on a Bruker X8 Quest CPAD area detector diffractometer, and data were collected using a IμS 3.0 Microfocus Mo−Kα radiation source (λ = 0.71073 Å) at cryogenic temperatures (100 K). Data reduction and absorption corrections were performed using the SAINT and SADABS software packages, respectively.[1] All structures were solved by direct methods and refined by full-matrix least-squares procedures on F2 , using the Bruker SHELXTL-2014 software package.[2-3] Non-hydrogen atoms were anisotropically refined, after which hydrogen atoms were introduced at calculated positions, and the data further refined. The graphical illustrations of crystal structures used throughout the main paper and the Supporting Information were created using the program VESTA, while the bond lengths and angles of the inorganic species were extracted using program Mercury.[4]

Analysis of structural distortions in pure low-dimensional perovskites. Distortion of the octahedral $[PbI_6]^{4-}$ inorganic building blocks of the materials were evaluated using the following parameters:

Bond length distortion:[5]

$$\Delta_{oct} = \frac{1}{6}\sum_{i=1}^{6}\left[\frac{d_i - d_m}{d_m}\right]^2 \quad \textbf{(Equation S1)}$$

Octahedral elongation:[6-7]

$$\lambda_{oct} = \frac{1}{6}\sum_{i=1}^{6}\left[\frac{d_i}{d_0}\right]^2 \quad \textbf{(Equation S2)}$$

Octahedral angle variance:[5-8]

$$\sigma^2_{oct} = \frac{1}{11}\sum_{i=1}^{12}(\alpha_i - 90)^2 \quad \textbf{(Equation S3)}$$

where d_i = Individual Pb–I bond length, d_m = average Pb–I bond length, d_0 = center-to-vertex distance of a regular polyhedron of the same volume, and α_i = individual I–Pb–I angles. The

parameters Δ_{oct}, λ_{oct} and σ^2_{oct} provide a quantitative measure of polyhedral distortion, independent of the effective size of the polyhedron. The software VESTA was used in calculation of λ_{oct} and σ^2_{oct}.

Raman Spectroscopy. Raman scattering measurements were performed using a WITec alpha 300RAS confocal Raman microscope. An Acton spectrometer with a diffraction grating of 1800 grooves mm^{-1} (1.3 cm^{-1} resolution) and a thermoelectrically cooled Andor CCD detector were used to collect data. To avoid absorption by the samples, which could lead to photoluminescence and degradation, the 633 nm (red) line from a He−Ne gas laser with a power of 5 mW was chosen, while the laser spot area was ~1 μm^2. The backscattered Raman signal passed through two 633 nm BragGrate Notch Filters (BNF).

Solid-state nuclear magnetic resonance (ss-NMR) spectroscopy. The experiments were completed on a 14.1 T Bruker Advance III HD 600 MHz spectrometer using a 1.9 mm Bruker HXY probe. All spectra were processed using the Topspin software package and referenced to the unified scale using IUPAC recommended frequency ratios relative to the ^{13}C adamantane$_{(s)}$ methylene resonance (δ = 37.77 ppm).[9-10] Spectral deconvolution was performed with dmfit.[11] Recycle delays sufficient for full relaxation were determined using saturation recovery pulse sequences with a 200 $\pi/2$ pulse saturation block. The ^{133}Cs NMR ($\upsilon_0(^{133}Cs)$ = 78.724 MHz) one-pulse experiments were acquired at an MAS frequency of 24 kHz, utilising a non-selective $\pi/2$ pulse of 6.5 μs (determined on $CsCl_{(s)}$), and a recycle delay of 60 s. The ^{207}Pb NMR ($\upsilon_0(^{207}Pb)$ = 125.60 MHz) Hahn-echo pulse experiments were acquired using at an MAS frequency of 24 kHz, utilising $\pi/2$ and π pulses of 4.125 and 8.25 μs (determined on $Pb(NO_3)_{2(s)}$), a recycle delay of 0.5 s, and a rotor synchronised echo delay of 35.48 μs. The ^{19}F NMR ($\upsilon_0(^{19}F)$ = 564.67 MHz) Hahn-echo pulse experiments were acquired using an MAS frequency of 24 kHz, utilising $\pi/2$ and π pulses of 3.5 and 7 μs, sample dependant recycle delays (10 – 180 s), and a rotor synchronised echo delay of 36.4 μs. The $^{13}C[^1H]$ NMR CP experiments were acquired at an MAS frequency of 12 kHz, utilising a 4000 μs contact pulse length, a ^1H $\pi/2$ pulse 1.85 μs (determined on adamantane$_{(s)}$), high power proton decoupling, and sample dependant recycle delays (5 - 20 s).

Morphological characterization

Field-emission scanning electron microscopy (FESEM). Surface morphology and cross-section images of the halide perovskite thin films and solar cell devices were recorded using a JEOL JSM-7600F FESEM, with an accelerating voltage of 5 kV.

Atomic force microscopy (AFM). AFM measurements were conducted using a Bruker Icon microscope. All measurements were performed in the standard tapping mode with OTESPA-R3 tips from Bruker.

Optical characterization

UV/Vis and steady-state photoluminescence (SSPL) spectroscopies. UV/Vis absorption and SSPL spectra were recorded using a SHIMADZU UV-3600 spectrophotometer (with an integrating sphere (ISR-3100) in the wavelength range 300–800 nm) and Horiba Fluoromax-3 spectrometer (with 450 nm excitation wavelength and 0.5 nm wavelength resolution), respectively.

Time-resolved photoluminescence (TRPL) spectroscopy. Samples were photoexcited with 450 nm femtosecond laser pulses, generated using an optical parametric amplifier (OPA, Coherent OPerA Solo). The OPA was powered by a Coherent LIBRA laser, with a fundamental wavelength of 800 nm and output pulse width of ∼50 fs, at a repetition rate of 1 kHz. The photoluminescence (PL) signal was collected using a lens pair and sent to a spectrometer (Princeton Instrument, SP-2500 series), where it was detected by a CCD camera (Pixis-400) or a streak camera (Optronis) in steadystate and time-resolved measurements, respectively. The experiments were carried out at room temperature on a glass substrate and the decay curve were fitted with a biexponential function in **Equation S4**:[12]

$$I(t) = I_0 + A_1 \exp^{-(t-t_0)/\tau_1} + A_2 \exp^{-(t-t_0)/\tau_2} \qquad \textbf{(Equation S4)}$$

Transient absorption (TA) spectroscopy. The measurements were performed using HELIOS (Ultrafast Systems, LLC) pump-probe setup in transmission mode. The 400-nm pump pulses were generated from a 1 kHz regenerative amplifier (Coherent Legend, 150 fs, 1 kHz, 800 nm,

1 mJ) passing through a BBO crystal by second-harmonic generation. The amplifier was seeded by a mode-locked Ti-sapphire oscillator (Coherent Vitesse, 80 MHz). The white light probe was generated by focusing 800 nm laser onto a 2-mm thick sapphire crystal. A 750-nm short-pass filter was placed before the probe focusing onto the sample. In addition, a 450-nm long-pass filter was used to block the excitation beam from entering the detector. By chopping the pump and adjusting the time delay between pump and probe, only pumped induced transmission change in the white light spectrum can be collected. The excitation fluence was 1.7 μJ/cm^2.

Photoluminescence quantum yield (PLQY). Samples were photoexcited with 450 nm femtosecond laser pulses, generated using an optical parametric amplifier (OPA, Coherent OPerA Solo). The OPA was powered by a Coherent LIBRA laser, with a fundamental wavelength of 800 nm and output pulse width of ~50 fs, at a repetition rate of 1 kHz and 2.5 μW.

Time-resolved UV/Vis spectroscopy. Kinetic experiments were performed using an Ailgent Cary 8454 diode-array spectrometer with an acquisition range of 190 to 1100 nm with a scan rate of 0.5 s. A 10 mm pathlength cuvette equipped with a stir-bar was charged with 2 mL of chlorobenzene at room temperature. Subsequently, 5 - 10 uL of 0.10 M perovskite precursor solution was injected to the cuvette using a 100 uL SGE gas tight syringe under stirring.

Compositional characterization

Thermogravimetric analysis. The thermal analyses were performed using a TA Instruments TGA Q2950 and Q500 models. Samples were heated from room temperature to 400 °C in nitrogen (N_2) with a heating rate of 5 °C/min and flow rate of 60 mL/min.

X-ray photoelectron spectroscopy (XPS). XPS studies were performed using an AXIS Supra spectrometer (Kratos Analytical Inc., UK), equipped with a hemispherical analyser, and a monochromatic Al K-alpha source (1487 eV) operated at 15 mA and 15 kV. The XPS spectra were acquired from an 700 x 300 μm^2 area, with a take-off angle of 90°. Pass energies of 160 eV and 20 eV were used for survey and high-resolution scans, respectively. The sample was depth-profiled using an Ar Gas Cluster Ion Source (GCIS, Kratos Analytical Inc., Minibeam 6) operated at 10 keV, Ar_{1000}^+, with a raster size of 2 x 2 mm^2. The XPS spectra were acquired

after progressive etch cycles of 30 s. The sample was electrically grounded to the sample holder to prevent charge build-up on the sample surface.

Device characterization

Solar cell devices efficiencies. Photovoltaic characteristics of the solar cell devices were measured in both reverse (from V_{OC} to J_{SC}) and forward (from J_{SC} to V_{OC}) scanning direction, with a sweep rate of 100 mV s^{-1}, un-der AM 1.5G (100 Mw cm^{-2}) spectral irradiation from a solar simulator (Newport 91190A) incorporating a 450 W xenon lamp (model 81172, Oriel) calibrated with a Si reference cell (Oriel PN91150). Devices were characterized through a 0.084 cm^2 black mask.

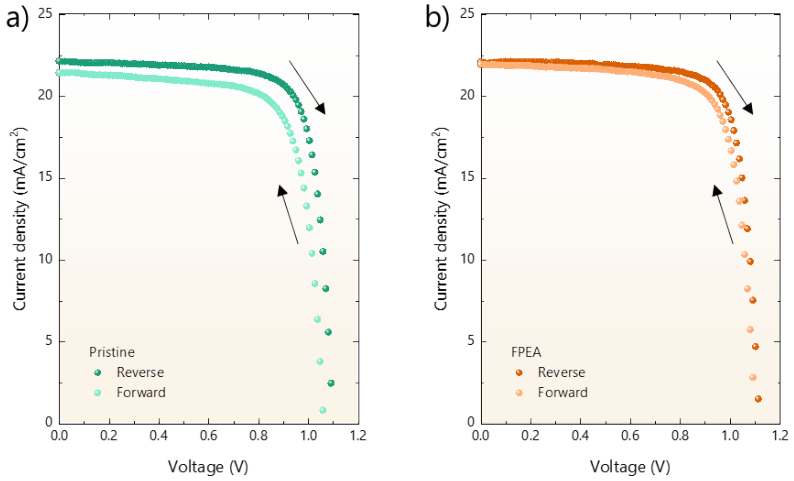

Figure S1. Typical current density−voltage (*J*−*V*) characteristics of best performing perovskite solar cells fabricated from precursor solution based on a) pristine $FA_{0.85}Cs_{0.15}PbI_3$ and b) with the addition of 2.5 mole% (relative to 3D perovskite) of cation FPEA in which the devices were subjected to forward and reverse bias scan directions.

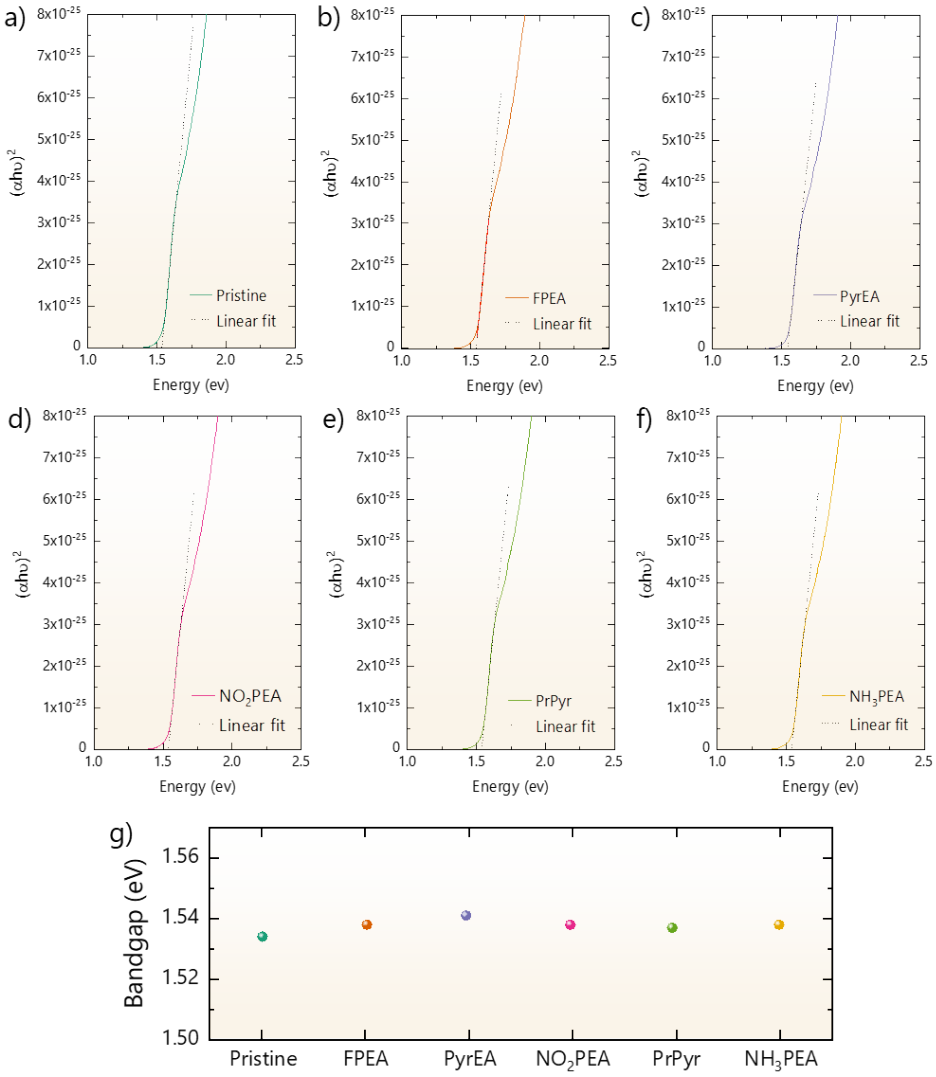

Figure S2. Tauc's plots (a-f) and band gap (derived from each of the plots; g) comparison across different perovskite materials fabricated from precursor solution based on pristine $FA_{0.85}Cs_{0.15}PbI_3$ and with the addition of 2.5 mole% (relative to 3D perovskite) of cations FPEA – NH_3PEA in which the values were derived from Tauc-plot of the corresponding UV-vis absorption spectra.

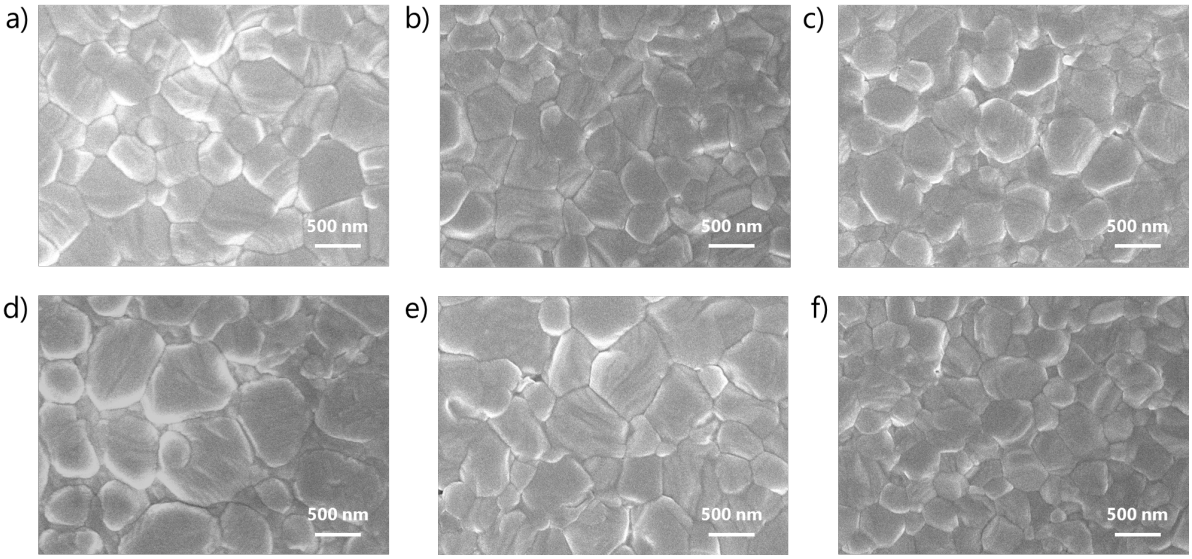

Figure S3. Top morphological scanning electron microscope images of perovskite thin films fabricated from precursor solutions based on a) pristine $FA_{0.85}Cs_{0.15}PbI_3$ and with the addition of 2.5 mole% (relative to 3D perovskite) of cations b) FPEA, c) PyrEA, d) NO_2PEA, e) PrPyr, and f) NH_3PEA.

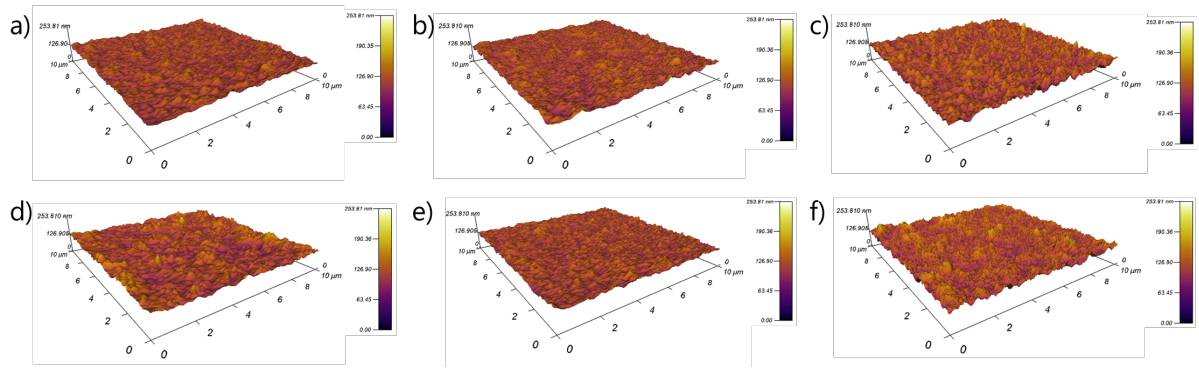

Figure S4. Topological images of the surfaces perovskite thin films fabricated from precursor solutions based on a) pristine $FA_{0.85}Cs_{0.15}PbI_3$ and with the addition of 2.5 mole% (relative to 3D perovskite) of cations b) FPEA, c) PyrEA, d) NO_2PEA, e) PrPyr, and f) NH_3PEA. The size of the atomic force microscopy (AFM) images is 10 x 10 μm^2.

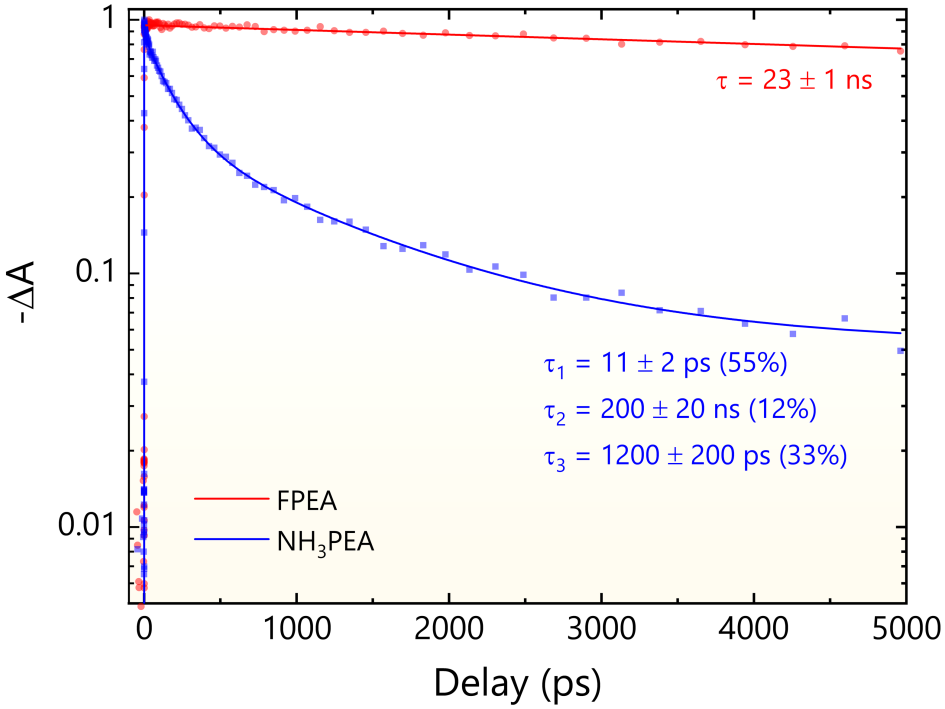

Figure S5. Fitted main bleaching peaks extracted from femtosecond transition absorption plots (**Figures 2e-f** in the main article) collected from mixed-dimensional perovskites based on cations FPEA and NH_3PEA. The result shows a single exponential decay exhibited by FPEA-added sample with a time constant of 23 ns (limited by our measurement range). Meanwhile, more significant quenching was observed in the case of NH_3PEA-added sample (fitted with tri-exponential decay) with an effective lifetime of 800 ps. As mentioned in the main article, this is consistent with our interpretation that defect passivation could only be achieved with cation FPEA, but not with NH_3PEA.

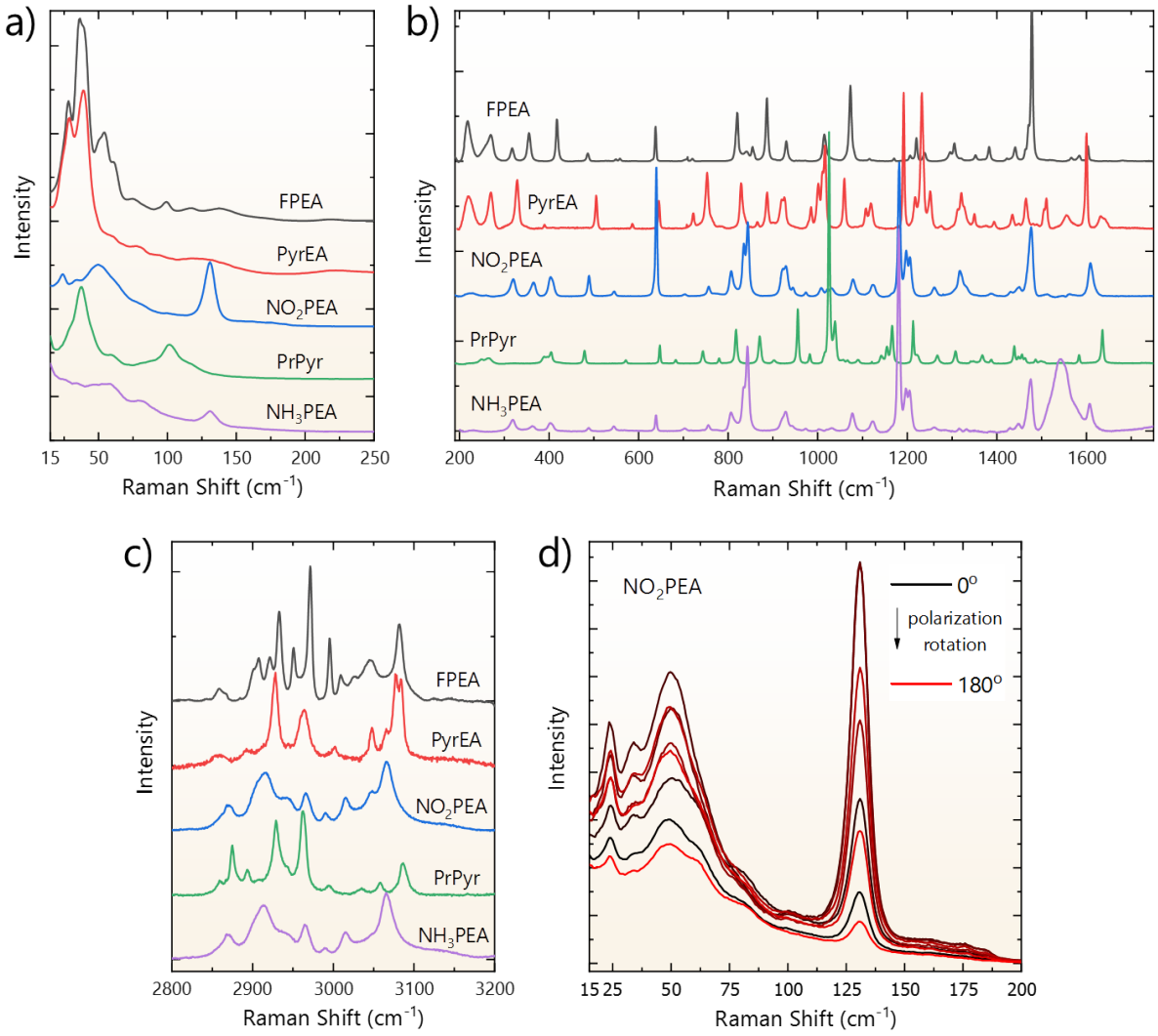

Figure S6. Figures a) to c) are the Raman spectra of pure low-dimensional perovskites based on cations FPEA – NH_3PEA recorded at various frequency regions. Analysis of the spectra is complicated due to a large number of overlapping peaks, but there are some clear features. First, the spectra profiles of most of the perovskites are different except those of $(FPEA)_2PbI_4$ and $(PyrEA)PbI_4$ exhibiting "flat" layered inorganic structures. Apart from the minor frequency shifts and the intensity of the 55 cm^{-1} feature they are similar, indicating the same motif of the octahedra connectivity.[13] The difference in the 55 cm^{-1} is likely due to the more tilted octahedra in $(PyrEA)PbI_4$. The octachedra are connected in a different way in the perovskites templated by NO_2PEA – NH_3PEA cations, causing significant changes in both frequencies and intensities of the Raman features. Additionally, in-plane Raman anisotropy behaviour was observed from the $(NO_2PEA)_2PbI_4$ sample. This is as expected because the material adopts a corrugated (110) "3 × 3" structure that would respond incident light differently depending on the orientations of the inorganic lattices.[14] Shown in Figure d) are the series of Raman spectra measured while changing the angle between the crystal orientation and polarisation of the excitation laser (180 degrees rotation). Intensity and the intensity ratio of the peaks are strongly angle dependent.

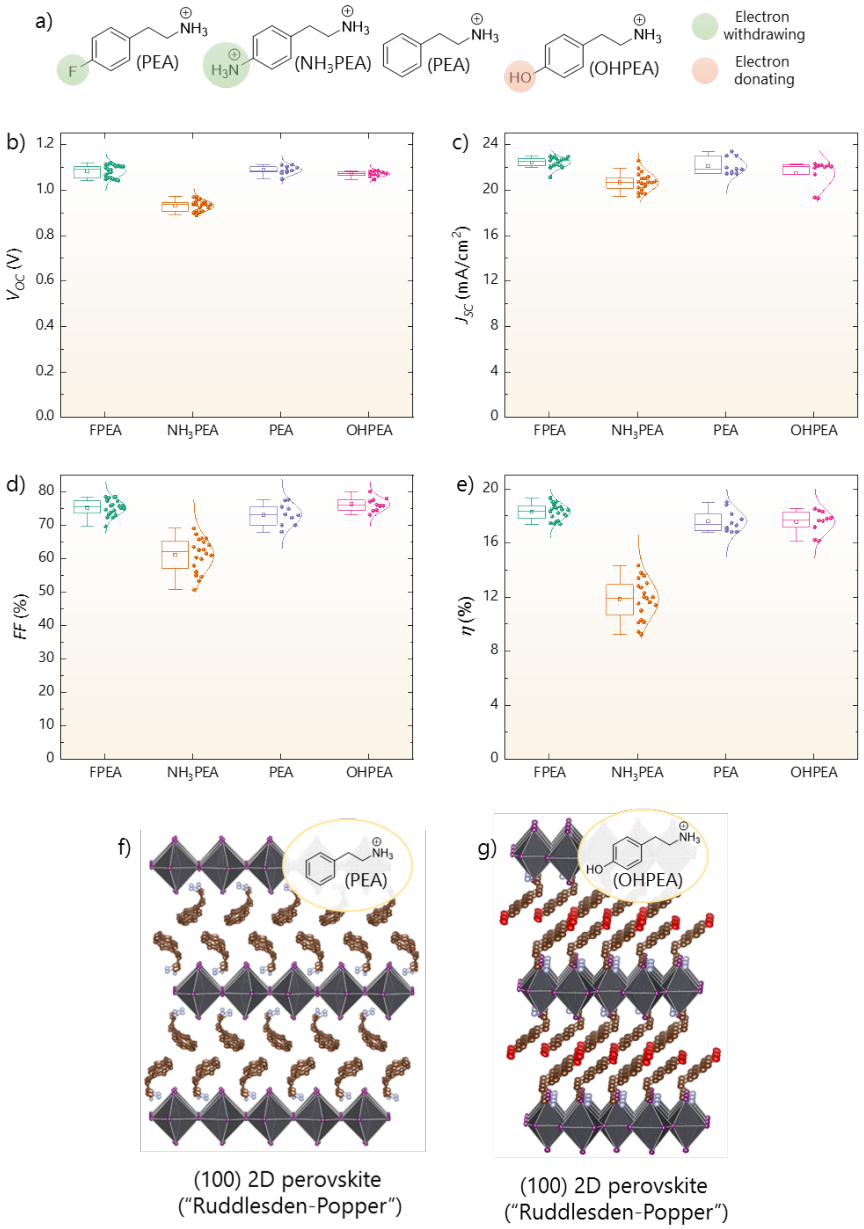

Figure S7. a) Molecular structures of organic templating cations where the *para*-functionality of the phenyl ring is modulated based on the electron affinity profile. Statistical representations of b) open circuit voltage (V_{OC}), c) short-circuit current (J_{SC}), d) fill factor (FF), and e) power conversion efficiency (PCE or η) measured for 10 – 20 photovoltaic devices, each for mixed-dimensional perovskites based on FPEA, NH_3PEA, PEA, and OHPEA. The photovoltaic parameters of each type of devices are summarized in **Tables S2, S6, S21, and S22**. X-ray crystal structures of (100) "Ruddlesden-Popper" 2D perovskites f) $(PEA)_2PbI_4$ and g) $(OHPEA)_2PbI_4$. Ellipsoids are shown at 50% probability. H atoms are omitted for clarity. Gray, purple, brown, red, and blue spheroids represent Pb, I, C, O, and N atoms, respectively. The insets show the molecular structures of the templating cations. Distortion parameters derived from the crystal structures are summarized in **Table S23** where the corresponding inorganic bond-lengths and bond-angles are listed in **Tables S11, S12, S19, S20, S24, S25, S26 and S27**.

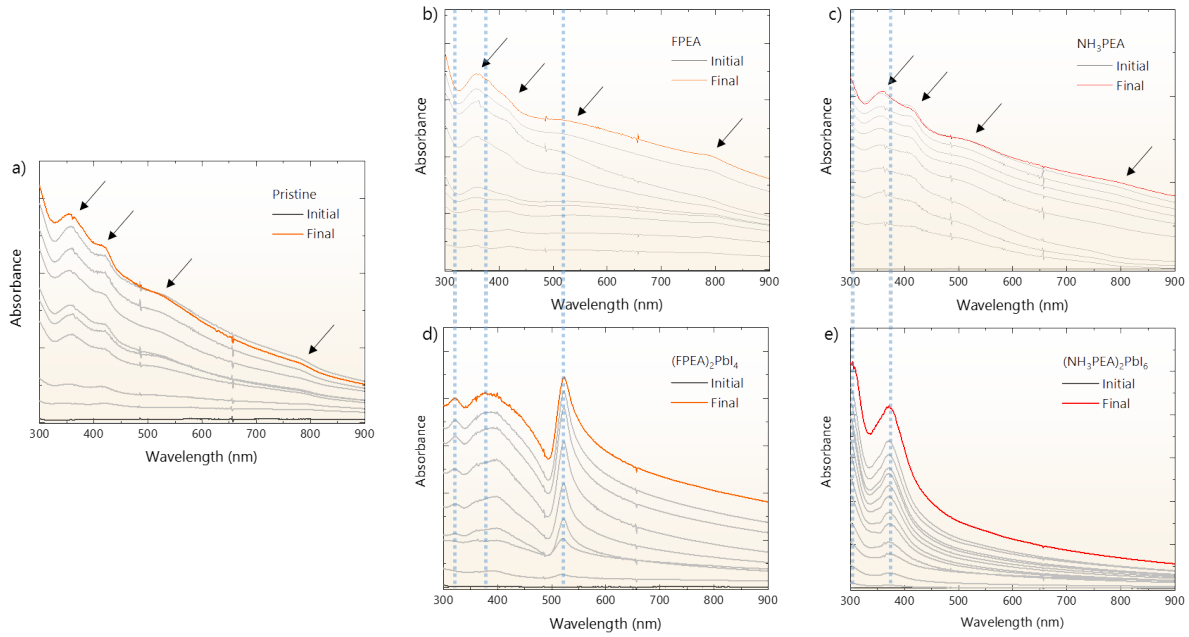

Figure S8. The absorbance spectra evolution against time of the chlorobenzene solution (acting as "anti-solvent") upon addition of perovskite precursors with various cations systems: a) pristine 3D $FA_{0.85}Cs_{0.15}PbI_3$, b) mixed-dimensional perovskite based on 2.5 mole% (relative to 3D perovskite) addition of cation FPEA, c) mixed-dimensional perovskite based on 2.5 mole% (relative to 3D perovskite) addition of cation NH_3PEA, d) pure low-dimensional perovskite $(FPEA)_2PbI_4$, and e) pure low-dimensional perovskite $(NH_3PEA)_2PbI_6$, illustrating the formation kinetics of the different compositions. Black arrows indicate the peaks belonging to 3D perovskites, while dotted blue line designate those of pure low-dimensional counterparts.

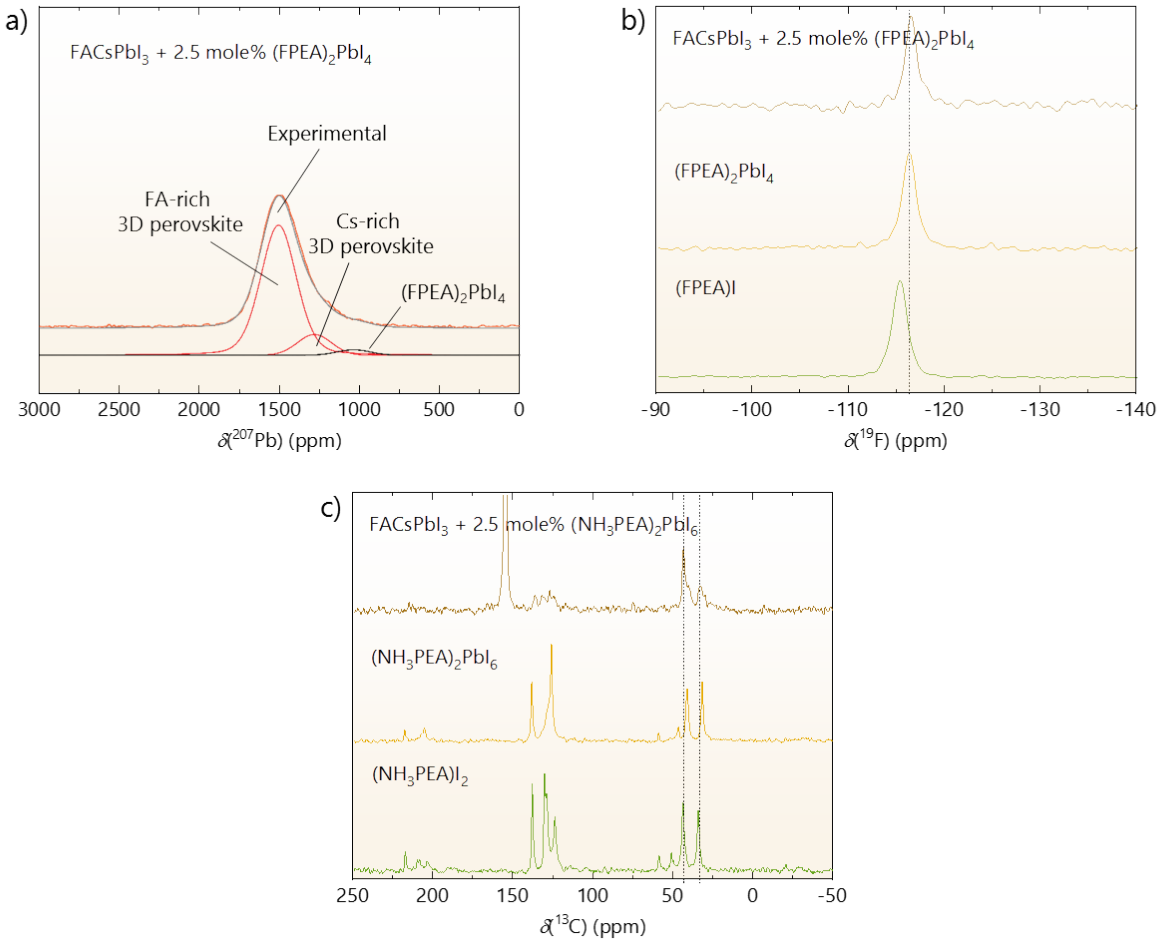

Figure S9. Solid-state nuclear magnetic resonance (NMR) spectra of mixed-dimensional perovskites based on cations FPEA and NH_3PEA investigated in this study. ^{207}Pb NMR spectra shown in Figure a) suggest that the final stoichiometric amount of low-dimensional perovskite $(FPEA)_2PbI_4$ in the thin film is similar to that of precursor solution. Meanwhile, the ^{19}F NMR spectra in figure b) indicate that the cation FPEA exists in the perovskite form rather than segregating into pure halide salt. Finally, since cation NH_3PEA is not functionalized with fluorine atoms, ^{13}C NMR spectroscopy was utilized to provide a strong evidence of perovskite $(NH_3PEA)_2PbI_6$ in the final film composition.

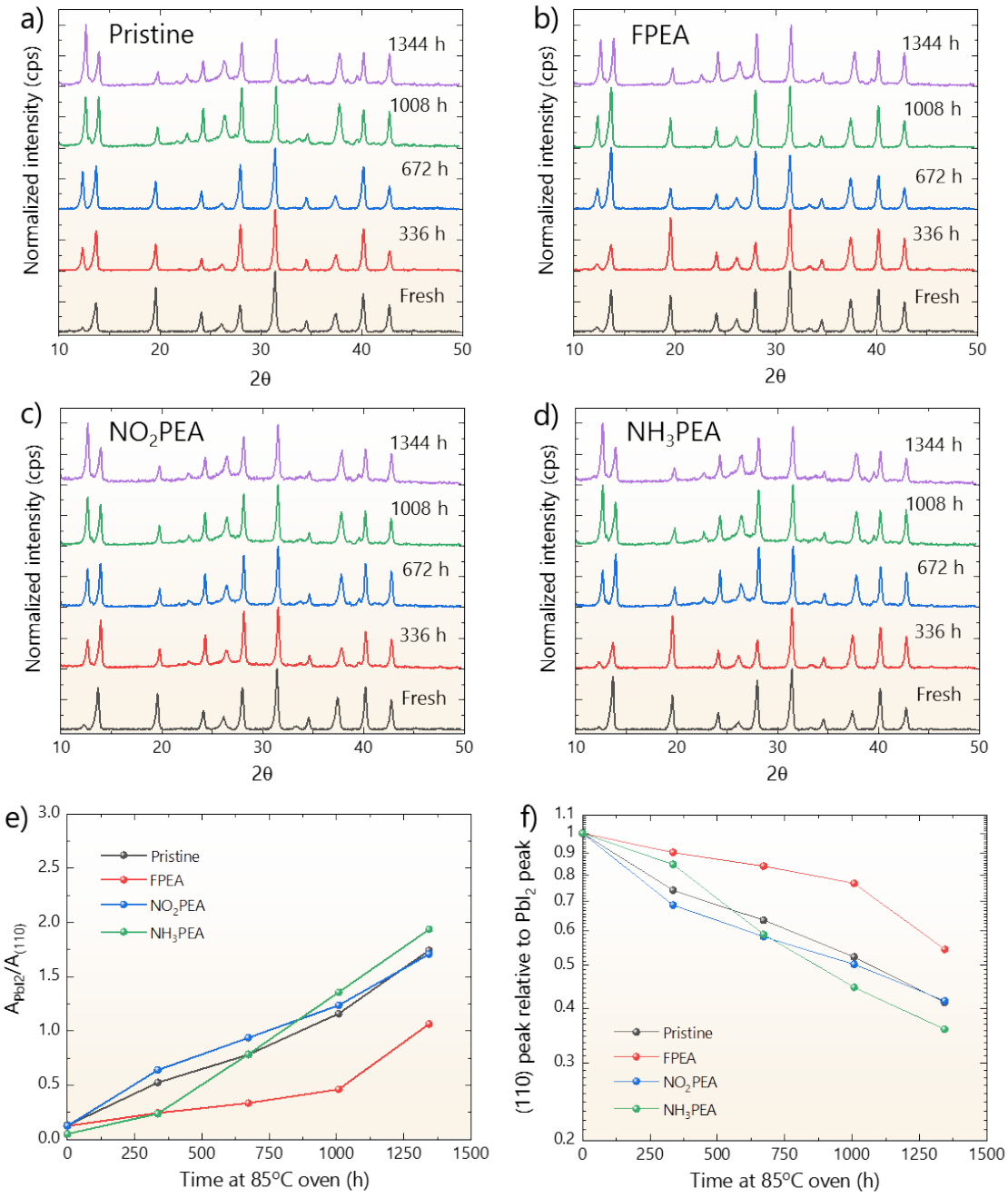

Figure S10. Evolution of glancing angle X-ray diffraction (XRD) patterns of perovskite thin films based on a) pristine 3D $FA_{0.85}Cs_{0.15}PbI_3$, b) 2.5 mole% (relative to 3D perovskite) addition of FPEA, c) 2.5 mole% (relative to 3D perovskite) addition of NO_2PEA, and d) 2.5 mole% (relative to 3D perovskite) addition of NH_3PEA upon subjecting the samples to thermal stability testing at 85°C and 10% relative humidity (RH) condition for more than 1200 hours. e) Ratio between the area under the curves belonging to those of (110) perovskite and PbI_2 peaks extracted from the corresponding XRD patterns and f) Normalized ratio between (110) perovskite peak relative to that of PbI_2 of different perovskite materials collected at different period during the thermal stability testing.

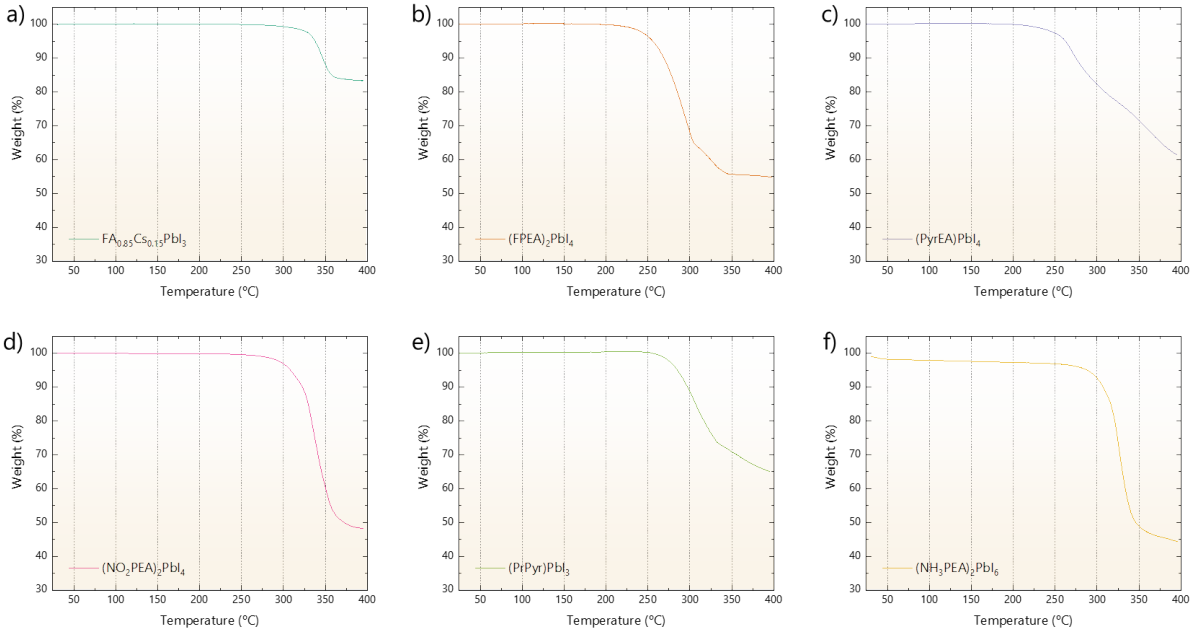

Figure S11. Thermal gravimetric analysis (TGA) of different perovskites a) 3D $FA_{0.85}Cs_{0.15}PbI_3$, b) 2D $(FPEA)_2PbI_4$, c) 2D $(PyrEA)PbI_4$, d) 2D $(NO_2PEA)_2PbI_4$, e) 1D $(PrPyr)PbI_3$, and 0D $(NH_3PEA)_2PbI_6$. The analysis suggests that three-dimensional perovskites may not necessarily thermally less-stable in comparison to those of low-dimensional counterpart. However, the presence of suitable low-dimensional perovskites which are able to passivate the defects in the grain boundaries of the 3D perovskites (thus improving the materials quality) and at the same time provides a hydrophobic effect to the materials contribute to the stability of the overall mixed-dimensional species towards moisture and heat.

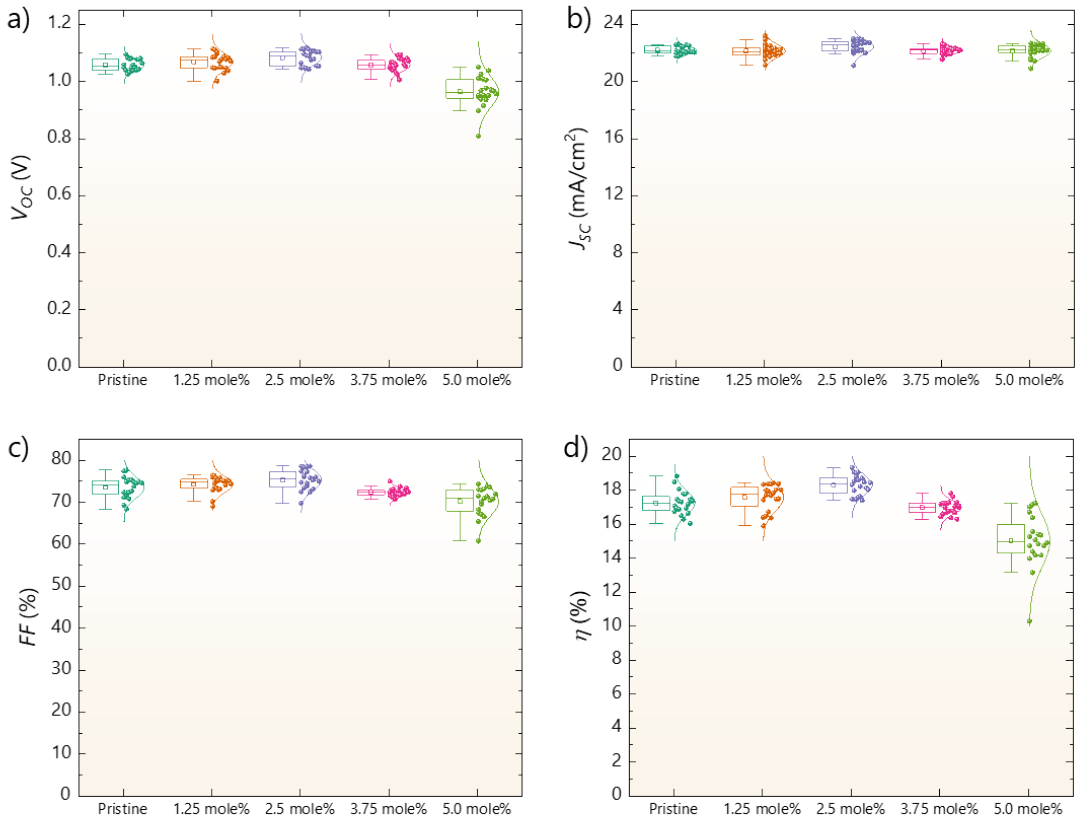

Figure S12. Photovoltaic parameters of the mixed-dimensional halide perovskite solar cells fabricated with different amount of 2D $(FPEA)_2PbI_4$ additive. The corresponding parameter values of each device are listed in **Tables S1-S2 and S28-S30**.

Table S1. Photovoltaic performance of devices fabricated from pure $FA_{0.85}Cs_{0.15}PbI_3$ precursor solutions.

Samples	V_{OC} (mV)	J_{SC} (mA/cm^2)	FF	η (%)
Device 1	1059	22.55	77.43	18.49
Device 2	1095	22.15	77.61	18.83
Device 3	1049	22.08	72.32	16.75
Device 4	1082	22.20	71.11	17.08
Device 5	1079	22.59	71.73	17.48
Device 6	1081	21.99	75.96	18.06
Device 7	1039	21.78	74.87	16.94
Device 8	1026	21.86	75.27	16.89
Device 9	1033	22.10	72.28	16.50
Device 10	1058	21.78	75.28	17.36
Device 11	1048	22.44	69.26	16.29
Device 12	1051	22.04	74.72	17.31
Device 13	1078	22.15	74.51	17.79
Device 14	1077	22.08	74.78	17.79
Device 15	1081	22.45	70.78	17.18
Device 16	1038	22.56	74.53	17.45
Device 17	1064	22.03	72.29	16.94
Device 18	1047	21.90	72.64	16.65
Device 19	1040	22.60	73.80	17.35
Device 20	1043	22.52	68.35	16.05

Table S2. Photovoltaic performance of devices fabricated from mixed-dimensional perovskite precursor solutions with 2.5 mole% (relative to 3D perovskite) addition of cation FPEA.

Samples	V_{OC} (mV)	J_{SC} (mA/cm^2)	FF	η (%)
Device 1	1065	21.97	74.68	17.47
Device 2	1097	22.62	72.48	17.98
Device 3	1091	22.87	73.42	18.32
Device 4	1090	22.97	69.73	17.45
Device 5	1113	22.12	78.52	19.34
Device 6	1114	22.13	77.37	19.07
Device 7	1119	21.13	78.31	18.52
Device 8	1113	22.23	75.99	18.80
Device 9	1104	22.78	73.92	18.59
Device 10	1107	22.52	76.22	19.00
Device 11	1076	22.59	72.34	17.58
Device 12	1079	22.66	74.51	18.22
Device 13	1048	22.73	78.49	18.70
Device 14	1055	22.28	78.58	18.48
Device 15	1054	22.24	77.27	18.12
Device 16	1049	22.17	75.80	17.63
Device 17	1047	22.73	73.14	17.40
Device 18	1043	22.95	75.27	18.02
Device 19	1103	22.00	75.97	18.44
Device 20	1104	23.00	75.04	19.05

Table S3. Photovoltaic performance of devices fabricated from mixed-dimensional perovskite precursor solutions with 2.5 mole% (relative to 3D perovskite) addition of cation PyrEA.

Samples	V_{OC} (mV)	J_{SC} (mA/cm^2)	FF	η (%)
Device 1	923	22.99	71.04	15.07
Device 2	908	22.37	70.09	14.24
Device 3	920	22.17	76.00	15.50
Device 4	929	22.14	74.75	15.38
Device 5	948	21.21	67.57	13.59
Device 6	1034	20.99	74.04	16.07
Device 7	1027	21.19	77.15	16.79
Device 8	1027	21.31	75.40	16.50
Device 9	1028	22.57	74.97	17.39
Device 10	983	22.73	64.43	14.40
Device 11	1018	20.99	74.45	15.91
Device 12	1055	21.44	69.09	15.63
Device 13	958	23.00	65.15	14.36
Device 14	1048	22.44	70.77	16.64
Device 15	1003	21.05	70.07	14.80
Device 16	983	22.43	65.74	14.50
Device 17	988	22.59	65.62	14.65
Device 18	1030	23.09	72.11	17.15
Device 19	1023	23.05	70.40	16.60
Device 20	1028	22.45	72.27	16.69

Table S4. Photovoltaic performance of devices fabricated from mixed-dimensional perovskite precursor solutions with 2.5 mole% (relative to 3D perovskite) addition of cation NO_2PEA.

Samples	V_{OC} (mV)	J_{SC} (mA/cm^2)	FF	η (%)
Device 1	934	21.74	70.98	14.41
Device 2	967	22.09	65.38	13.97
Device 3	968	21.65	65.12	13.65
Device 4	910	22.40	75.94	15.48
Device 5	966	21.97	68.22	14.48
Device 6	975	21.98	68.41	14.66
Device 7	981	22.16	66.47	14.45
Device 8	979	22.14	67.89	14.71
Device 9	974	22.47	66.22	14.48
Device 10	968	22.23	69.94	15.05
Device 11	1004	21.23	70.14	14.94
Device 12	1002	21.73	69.46	15.13
Device 13	875	22.09	72.43	14.00
Device 14	897	22.63	70.97	14.41
Device 15	894	22.70	73.98	15.01
Device 16	890	22.67	73.41	14.81
Device 17	966	22.55	70.33	15.32
Device 18	963	22.12	71.39	15.21
Device 19	962	22.45	68.33	14.75
Device 20	975	21.64	65.86	13.89

Table S5. Photovoltaic performance of devices fabricated from mixed-dimensional perovskite precursor solutions with 2.5 mole% (relative to 3D perovskite) addition of cation PrPyr.

Samples	V_{OC} (mV)	J_{SC} (mA/cm^2)	FF	η (%)
Device 1	901	21.51	71.55	13.87
Device 2	875	20.71	71.65	12.98
Device 3	988	22.05	63.85	13.90
Device 4	981	21.83	64.42	13.79
Device 5	909	21.20	66.16	12.75
Device 6	887	21.43	63.78	12.12
Device 7	882	21.37	72.43	13.65
Device 8	888	19.81	69.54	12.24
Device 9	964	21.31	64.63	13.29
Device 10	933	20.59	61.38	11.80
Device 11	943	21.07	58.53	11.62
Device 12	936	21.65	60.37	12.23
Device 13	982	21.85	62.86	13.48
Device 14	978	21.19	60.98	12.63
Device 15	920	22.31	70.48	14.47
Device 16	914	21.76	70.41	14.00
Device 17	969	22.70	62.09	13.66
Device 18	929	22.55	54.15	11.34
Device 19	958	21.14	60.32	12.21
Device 20	986	21.05	64.43	13.37

Table S6. Photovoltaic performance of devices fabricated from mixed-dimensional perovskite precursor solutions with 2.5 mole% (relative to 3D perovskite) addition of cation NH_3PEA.

Samples	V_{OC} (mV)	J_{SC} (mA/cm^2)	FF	η (%)
Device 1	936	20.72	69.15	13.41
Device 2	935	21.91	67.37	13.81
Device 3	943	21.37	63.60	12.82
Device 4	953	21.65	65.77	13.58
Device 5	902	20.59	50.81	9.44
Device 6	908	21.03	60.45	11.54
Device 7	899	20.50	55.00	10.13
Device 8	902	21.03	58.00	11.00
Device 9	924	20.72	62.70	12.00
Device 10	937	21.16	60.04	11.90
Device 11	960	22.59	66.20	14.35
Device 12	938	19.74	62.79	11.63
Device 13	970	20.65	65.06	13.03
Device 14	972	19.78	66.12	12.72
Device 15	890	19.47	53.42	9.25
Device 16	908	20.22	56.14	10.31
Device 17	925	20.08	54.64	10.15
Device 18	937	20.78	61.59	11.99
Device 19	941	20.37	64.15	12.30
Device 20	950	19.66	61.01	11.40

Table S7. Photovoltaic performance of devices fabricated from pristine $FA_{0.85}Cs_{0.15}PbI_3$ and mixed-dimensional perovskite precursor solutions with 2.5 mole% (relative to 3D perovskite) addition of cation FPEA where the devices are subjected to reverse and forward bias scan.

Samples	Scan direction	V_{OC} (V)	J_{SC} (mA/cm^2)	FF	η (%)
Pristine	Reverse	1.09	22.15	0.78	18.83
Pristine	Forward	1.06	21.47	0.74	16.84
FPEA	Reverse	1.11	22.11	0.79	19.38
FPEA	Forward	1.10	21.97	0.76	18.36

Table S8. Peak assignment of glancing-angle X-ray diffractometry patterns of halide perovskite samples presented in **Figure 2b**. The assignment follows the data reported in refs. 15–17.

2θ angle (degree)	Species
12.61	PbI_2
13.93	Perovskite (100)
19.77	Perovskite (110)
24.29	Perovskite (111)
28.13	Perovskite (200)
31.55	Perovskite (210)
34.67	Perovskite (112)
40.23	Perovskite (220)
42.75	Perovskite (300)

Table S9. Photoluminescence quantum yield (PLQY) values of pristine 3D $FA_{0.85}Cs_{0.15}PbI_3$ and mixed-dimensional perovskites based on cations FPEA – NH_3PEA.

Material	PLQY (%)
Pristine	3
2.5 mole% FPEA	11
2.5 mole% PyrEA	~ 1
2.5 mole% NO_2PEA	~ 1
2.5 mole% PrPyr	< 1
2.5 mole% NH_3PEA	< 1

Table S10. Summary of the time-resolved photoluminescence (TRPL) parameters of pristine 3D $FA_{0.85}Cs_{0.15}PbI_3$ and mixed-dimensional perovskites based on cations FPEA – NH_3PEA.

Parameters	Samples					
	Pristine	FPEA	PyrEA	NO_2PEA	PrPyr	NH_3PEA
PL decay τ_1 (ns)	3 (59 %)	5 (31 %)	3 (63 %)	4 (67%)	2 (52 %)	2 (79 %)
PL decay τ_2 (ns)	159 (41 %)	171 (69 %)	118 (37%)	130 (33 %)	29 (48 %)	33 (21 %)
PL decay τ_{ave} (ns)	68	118	46	45	15	10

Table S11. Metal–halide bond lengths (Å) in 2D $(FPEA)_2[PbI_4]$. The single crystal structure is obtained from ref.[18] Red and black colors indicate bonding with terminal and bridging halides, respectively.

Pb1–I1	3.168
Pb1–I1	3.171
Pb1–I2	3.221

Table S12. Halide–metal–halide bond angles (°) in 2D $(FPEA)_2[PbI_4]$. The single crystal structure is obtained from ref. [18] Red and black colors indicate *cis*- and *trans*- angles, respectively.

I2-Pb1–I1	90.36	I2-Pb1–I2	180
I2-Pb1-I1	93.24	I1-Pb1-I1	180
I2-Pb1-I1	89.64	I1-Pb1-I1	180
I2-Pb1–I1	86.76		
I1-Pb1–I1	88.92		
I1-Pb1-I1	91.08		

Table S13. Metal–halide bond lengths (Å) in 2D (PyrEA)[PbI_4]. Red and black colors indicate bonding with terminal and bridging halides, respectively.

Pb1–I1	3.183	Pb1–I2	3.249
Pb1–I1	3.223	Pb1–I4	3.123
Pb1–I3	3.194		
Pb1–I3	3.174		

Table S14. Halide–metal–halide bond angles (°) in 2D (PyrEA)[PbI_4]. Red and black colors indicate *cis*- and *trans*- angles, respectively.

I1-Pb1–I2	87.15	I2-Pb1–I3	96.75	I1-Pb1–I1	176.96
I1-Pb1-I3	91.57	I2-Pb1-I3	83.04	I2-Pb1-I4	173.86
I1-Pb1-I3	89.69	I3-Pb1-I4	92.91	I3-Pb1-I3	178.71
I1-Pb1–I4	88.35	I3-Pb1-I4	87.40		
I1-Pb1–I2	92.41				
I1-Pb1-I3	91.37				
I1-Pb1-I3	87.37				
I1-Pb1–I4	92.30				

Table S15. Metal–halide bond lengths (Å) in 2D ($NO_2PEA)_2$[PbI_4]. The single crystal structure is obtained from ref. [19] Red and black colors indicate bonding with terminal and bridging halides, respectively.

Pb1–I1	3.180	Pb3–I2	3.116
Pb1–I2B	3.186	Pb3–I2B	3.381
Pb1–I3	3.210	Pb3-I5	3.334
Pb2–I3	3.224	Pb3-I7	3.045
Pb2–I4	3.134	Pb3-I0AA	3.252
Pb2–I5	3.190	Pb3-I0AA	3.191

Table S16. Halide–metal–halide bond angles (°) in 2D $(NO_2PEA)_2[PbI_4]$. The single crystal structure is obtained from ref. [19] Red and black colors indicate *cis*- and *trans*- angles, respectively.

I1-Pb1–I2B	93.43	I0AA-Pb3–I7	94.88	I1-Pb1–I1	180.00
I1-Pb1-I2B	86.57	I0AA-Pb3-I2	85.17	I2B-Pb1-I2B	180.00
I1-Pb1-I3	93.21	I0AA-Pb3-I5	93.18	I3-Pb1-I3	180.00
I1-Pb1–I3	86.79	I0AA-Pb3-I2B	84.12	I3-Pb2-I3	180.00
I2B-Pb1–I3	92.41	I0AA-Pb3-I2B	83.36	I4B-Pb2-I4B	180.00
I3-Pb1-I2B	87.59	I0AA-Pb3-I2	101.70	I5-Pb2-I5	180.00
I3-Pb2-I4B	85.62	I0AA-Pb3-I5	79.80	I0AA-Pb3-I0AA	165.82
I3-Pb2-I4B	94.38	I0AA-Pb3-I7	97.98	I2B-Pb3-I7	176.65
I3-Pb2-I5	90.32	I2-Pb3-I7	85.52	I2-Pb3-I5	178.26
I3-Pb2-I5	89.68	I7-Pb3-I5	95.16		
I4B-Pb2-I5	92.10	I5-Pb3-I2B	88.08		
I5-Pb2-I4B	87.90	I2B-Pb3-I2	91.21		

Table S17. Metal–halide bond lengths (Å) in 1D (PrPyr)$[PbI_3]$. Red and black colors indicate bonding with terminal and bridging halides, respectively.

Pb1–I1	3.149
Pb1–I1	3.312
Pb1–I2	3.153
Pb1–I2	3.363

Table S18. Halide–metal–halide bond angles (°) in 1D (PrPyr)$[PbI_3]$. Red and black colors indicate *cis*- and *trans*- angles, respectively.

I1-Pb1–I1	89.76	I1-Pb1–I1	176.24
I1-Pb1-I1	92.92	I2-Pb1-I2	174.96
I1-Pb1-I1	84.29		
I1-Pb1-I2	83.47		
I1-Pb1–I2	92.97		
I1-Pb1-I2	99.46		
I1-Pb1–I2	84.25		

Table S19. Metal–halide bond lengths (Å) in 0D $(NH_3PEA)_2[PbI_6]$. Red and black colors indicate bonding with terminal and bridging halides, respectively.

Pb1–I1	3.283
Pb1–I2	3.477
Pb1–I3	2.945

Table S20. Halide–metal–halide bond angles (°) in 0D $(NH_3PEA)_2[PbI_6]$. Red and black colors indicate *cis*- and *trans*- angles, respectively.

I1-Pb1–I1	89.97	I1-Pb1–I1	177.22
I1-Pb1-I2	88.61	I2-Pb1-I3	180.00
I1-Pb1-I3	91.39		

Table S21. Photovoltaic performance of devices fabricated from mixed-dimensional perovskite precursor solutions with 2.5 mole% (relative to 3D perovskite) addition of cation PEA.

Samples	V_{OC} (mV)	J_{SC} (mA/cm^2)	FF	η (%)
Device 1	1111	21.97	70.14	17.12
Device 2	1082	23.02	75.61	18.83
Device 3	1049	23.42	77.50	19.03
Device 4	1075	21.45	73.33	16.92
Device 5	1079	21.63	74.94	17.48
Device 6	1084	21.47	72.31	16.83
Device 7	1087	21.48	77.74	18.14
Device 8	1098	21.86	70.08	16.82
Device 9	1103	23.03	68.07	17.30
Device 10	1113	21.83	73.07	17.75

Table S22. Photovoltaic performance of devices fabricated from mixed-dimensional perovskite precursor solutions with 2.5 mole% (relative to 3D perovskite) addition of cation OHPEA.

Samples	V_{OC} (mV)	J_{SC} (mA/cm^2)	FF	η (%)
Device 1	1075	22.33	17.72	18.54
Device 2	1069	22.15	17.57	18.39
Device 3	1082	22.20	17.50	18.31
Device 4	1065	22.02	16.42	17.18
Device 5	1060	21.98	16.88	17.67
Device 6	1086	21.40	16.85	17.64
Device 7	1078	22.20	17.01	17.80
Device 8	1085	22.06	17.05	17.84
Device 9	1047	19.34	15.51	16.23
Device 10	1074	19.26	15.43	16.15

Table S23. Distortion parameters derived from the single crystal X-ray structures of low-dimensional perovskites based on cations FPEA, NH_3PEA, PEA, and OHPEA.

Compound	Δd (x10^4)[b]	λ_{oct}[c]	σ_{oct}^2[d]
$(FPEA)_2PbI_4$	0.58	1.0013	4.29
$(NH_3PEA)_2PbI_6$	23.23	1.0028	1.41
$(PEA)_2PbI_4$[α]	0.61	1.0009	2.80
$(OHPEA)_2PbI_4$[α]	0.70	1.0004	1.12

[α]Averaged distortion parameters are given for $(PEA)_2PbI_4$ and $(OHPEA)_2PbI_4$ as they contain more than one geometrically distinct octahedrons. [b]Octahedral bond length distortion, [c]Octahedral elongation. [d]Octahedral angle variance

Table S24. Metal–halide bond lengths (Å) in 2D $(PEA)_2[PbI_4]$. Red and black colors indicate bonding with terminal and bridging halides, respectively.

Pb1–I1	3.218	Pb2-I3	3.187
Pb1–I2	3.193	Pb2-I4	3.213
Pb1–I3	3.154	Pb2-I5	3.200
Pb1-I6	3.185	Pb2-I6	3.159
Pb1-I7	3.154	Pb2-I7	3.156
Pb1-I8	3.154	Pb2-I8	3.143

Table S25. Halide–metal–halide bond angles (°) in 2D $(PEA)_2[PbI_4]$. Red and black colors indicate *cis*- and *trans*- angles, respectively.

I1-Pb1–I3	92.66	I3-Pb1–I8	89.62
I1-Pb1-I6	86.98	I3-Pb1-I7	91.06
I1-Pb1-I7	89.12	I6-Pb1-I7	88.98
I1-Pb1-I8	90.64	I6-Pb1-I8	90.34
I2-Pb1–I3	87.74	I4-Pb2–I7	92.06
I2-Pb1-I6	92.61	I7-Pb2–I5	87.48
I2-Pb1–I7	90.84	I5-Pb2–I8	92.93
I2-Pb1–I8	89.39	I8-Pb2–I4	87.52
I3-Pb2–I4	89.23	I1-Pb1-I2	179.59
I3-Pb2–I5	90.42	I3-Pb1-I6	179.64
I3-Pb2–I7	88.84	I7-Pb1-I8	179.29
I3-Pb2–I8	90.55	I3-Pb2–I6	179.40
I6-Pb2–I4	90.22	I4-Pb2–I5	179.43
I6-Pb2–I5	90.13	I7-Pb2–I8	179.26
I6-Pb2–I8	89.67		
I6-Pb2–I7	90.94		

Table S26. Metal–halide bond lengths (Å) in 2D $(OHPEA)_2[PbI_4]$. Red and black colors indicate bonding with terminal and bridging halides, respectively.

Pb1–I1	3.218	Pb2–I3	3.218
Pb1–I2	3.153	Pb2–I2	3.154
Pb1–I4	3.176	Pb2–I4	3.177

Table S27. Halide–metal–halide bond angles (°) in 2D $(OHPEA)_2[PbI_4]$. Red and black colors indicate *cis*- and *trans*- angles, respectively.

I1-Pb1–I2	90.66	I1-Pb1–I1	180.00
I1-Pb1-I1	89.34	I2-Pb1-I2	180.00
I1-Pb1-I4	88.40	I4-Pb1-I4	180.00
I1-Pb1-I4	91.60	I2-Pb2-I2	180.00
I2-Pb1–I4	89.64	I3-Pb2-I3	180.00
I4-Pb1-I2	90.36	I4-Pb2-I4	180.00
I3-Pb2–I2	90.57		
I3-Pb2–I2	89.43		
I3-Pb2–I4	88.38		
I3-Pb2–I4	91.62		
I2-Pb2–I4	89.71		
I4-Pb2–I2	90.29		

Table S28. Photovoltaic performance of devices fabricated from mixed-dimensional perovskite precursor solutions with 1.25 mole% of 2D $(FPEA)_2PbI_4$ additive.

Samples	V_{OC} (mV)	J_{SC} (mA/cm^2)	FF	η (%)
Device 1	1049	22.65	69.06	16.41
Device 2	1047	22.43	70.16	16.48
Device 3	1085	22.12	76.43	18.34
Device 4	1002	21.76	72.94	15.90
Device 5	1086	21.84	75.93	18.01
Device 6	1096	21.97	76.32	18.38
Device 7	1070	21.88	74.50	17.43
Device 8	1115	21.75	75.72	18.36
Device 9	1112	22.06	75.15	18.43
Device 10	1103	21.17	75.80	17.70
Device 11	1050	23.19	73.70	17.94
Device 12	1050	22.95	73.39	17.68
Device 13	1030	22.26	72.98	16.73
Device 14	1079	22.23	75.20	18.03
Device 15	1087	22.51	75.11	18.38
Device 16	1078	22.32	74.09	17.82
Device 17	1083	22.097	75.21	18.00
Device 18	1048	22.24	75.01	17.48
Device 19	1039	21.54	73.17	16.36
Device 20	1071	21.96	74.36	17.49

Table S29. Photovoltaic performance of devices fabricated from mixed-dimensional perovskite precursor solutions with 3.75 mole% of 2D $(FPEA)_2PbI_4$ additive.

Samples	V_{OC} (mV)	J_{SC} (mA/cm^2)	FF	η (%)
Device 1	1047	21.93	71.59	16.43
Device 2	1044	21.971	72.37	16.60
Device 3	1040	22.41	72.90	16.99
Device 4	1053	22.25	71.23	16.70
Device 5	1044	21.94	73.14	16.75
Device 6	1032	21.95	72.33	16.38
Device 7	1069	22.19	72.39	17.18
Device 8	1067	22.21	72.71	17.24
Device 9	1065	21.57	74.98	17.22
Device 10	1057	22.08	73.73	17.21
Device 11	1092	22.22	71.17	17.27
Device 12	1081	21.95	70.68	16.77
Device 13	1024	22.61	72.05	16.68
Device 14	1006	22.38	72.48	16.29
Device 15	1095	22.59	72.02	17.81
Device 16	1077	22.30	73.38	17.62
Device 17	1061	22.25	71.92	16.99
Device 18	1053	22.34	72.45	17.05
Device 19	1082	22.26	71.77	17.28
Device 20	1072	22.22	71.73	17.09

Table S30. Photovoltaic performance of devices fabricated from mixed-dimensional perovskite precursor solutions with 5.0 mole% of 2D $(FPEA)_2PbI_4$ additive.

Samples	V_{OC} (mV)	J_{SC} (mA/cm^2)	FF	η (%)
Device 1	809	20.91	60.80	10.29
Device 2	946	22.07	73.02	15.24
Device 3	952	21.64	71.48	14.72
Device 4	969	22.05	72.87	15.56
Device 5	952	22.17	68.21	14.39
Device 6	977	21.50	67.48	14.17
Device 7	938	22.22	67.09	13.98
Device 8	951	22.48	69.44	14.83
Device 9	898	22.00	66.56	13.15
Device 10	1011	21.43	65.43	14.17
Device 11	970	22.16	70.09	15.07
Device 12	967	22.45	70.95	15.40
Device 13	915	22.54	71.40	14.72
Device 14	1025	22.68	73.18	17.02
Device 15	936	22.60	70.38	14.90
Device 16	1009	22.46	73.78	16.72
Device 17	957	22.66	70.79	15.35
Device 18	1051	22.19	73.51	17.15
Device 19	1006	22.65	71.92	16.38
Device 20	1038	22.32639	74.37	17.24

References

1. SAINT and SADABS; Bruker AXS Inc.: Madison, WI, (2007).
2. Sheldrick, G. M. SHELXL-97, Program for crystal structure refinement; Göttingen, 1997.
3. Sheldrick, G. M. Acta Crystallogr., *Sect. A: Found. Crystallogr.* **2008**, *64*, 112–122.
4. Momma, K.; Izumi, F., An Integrated Three-Dimensional Visualization System VESTA Using wxWidgets. *Commission on Crystallogr. Comput.* **2006**, *7*, 106–119.
5. Ertl, A.; Hughes, J. M.; Pertlik, F.; Jr., F. F. F.; Wright, S. E.; Brandstatter, F.; Marler, B. Polyhedron Distortions in Tourmaline. *Can. Mineral.,* **2002**, *40*, 153–162.
6. Robinson, K.; Gibbs, G. V.; Ribbe, P. H. Quadratic Elongation: A Quantitative Measure of Distortion in Coordination Polyhedra. *Science* **1971**, *172*, 567–570.
7. Thomas, N. W. Crystal Structure-Physical Property Relationships in Perovskites. *Acta Crystallogr. B* **1989**, *45*, 337–344.
8. Fleet, M. E. Distortion Parameters for Coordination Polyhedra. *Mineral. Mag.* **1976**, *40*, 531–533.
9. Harris, R. K.; Becker, E. D.; Cabral De Menezes, S. M.; Goodfellow R.; Granger, P. NMR Nomenclature: Nuclear Spin Properties and Conventions for Chemical Shifts (IUPAC Recommendations 2001), *International Union of Pure and Applied Chemistry*, **2002**, *1*, 43–64.
10. Harris, R. K.; Becker, E. D.; Cabral de Menezes, S. M.; Granger, P.; Hoffman, R. E.; Zilm, K. W. Further conventions for NMR shielding and chemical shifts (IUPAC Recommendations 2008), *Pure Appl. Chem.*, **2008**, *80*, 59–84.
11. Massiot, D.; Fayon, F.; Capron, M.; King, I.; Le Calvé, S.; Alonso, B.; Durand, J.-O.; Bujoli, B.; Gan Z.; Hoatson, G. Modelling one- and two-dimensional solid-state NMR spectra: Modelling 1D and 2D solid-state NMR spectra, *Mag. Res. Chem,*, **2002**, *40*, 70–76.
12. J, Li., *et al.*, Highly Efficient Thermally Co-evaporated Perovskite Solar Cells and Mini-modules. *Joule* **2020**, *4*, 1035-1053.
13. Dhanabalan, B.; Castelli, A.; Palei, M.; Spirito, D.; Manna, L.; Krahne, R.; Arciniegas, M., Simple fabrication of layered halide perovskite platelets and enhanced photoluminescence from mechanically exfoliated flakes. *Nanoscale* **2019**, *11* (17), 8334-8342.

14. Lekina, Y.; Febriansyah, B.; Fan, X.; You, L.; Morris, S.; Wang, J.; England, J.; Huang, X.; Yan, J.; Shen, Z. X., Strong Optical, Electrical, and Raman in-Plane Anisotropy in Corrugated Two-Dimensional Perovskite. *J. Phys. Chem. C* **2021**, *125* (41), 22630-22642.
15. Zhou, N., *et. al.,* CsI Pre-Intercalation in the Inorganic Framework for Efficient and Stable $FA_{1-x}Cs_xPbI_3(Cl)$ Perovskite Solar Cells. *Small* **2017**, *13*, 1700484(1–9).
16. Cordero, F., *et. al.,* Stability of Cubic $FAPbI_3$ from X-ray Diffraction, Anelastic, and Dielectric Measurements. *J. Phys. Chem. Lett.* **2019**, *10* (10), 2463–2469.
17. Murugadoss, G., *et. al.,* Crystal stabilization of α-$FAPbI_3$ perovskite by rapid annealing method in industrial scale. *J. Mater. Res. Tech.* **2021**, *12*, 1924e1930.
18. Hu, J.; Oswald, I. W. H.; Stuard, S. J.; Nahid, M. M.; Zhou, N.; Williams, O. F.; Guo, Z.; Yan, L.; Hu, H.; Chen, Z.; Xiao, X.; Lin, Y.; Yang, Z.; Huang, J.; Moran, A. M.; Ade, H.; Neilson, J. R.; You, W., Synthetic control over orientational degeneracy of spacer cations enhances solar cell efficiency in two-dimensional perovskites. *Nat. Commun.* **2019,** *10* (1), 1276.
19. Tremblay, M. H.; Thouin, F.; Leisen, J.; Bacsa, J.; Srimath Kandada, A. R.; Hoffman, J. M.; Kanatzidis, M. G.; Mohite, A. D.; Silva, C.; Barlow, S.; Marder, S. R., $(4NPEA)_2PbI_4$ (4NPEA = 4-Nitrophenylethylammonium): Structural, NMR, and Optical Properties of a 3 x 3 Corrugated 2D Hybrid Perovskite. *J. Am. Chem. Soc.* **2019,** *141* (11), 4521-4525.